ACS APPLIED MATERIALS & INTERFACES

Research Article

www.acsami.org

Evaluation of the Segregation of Paramagnetic Impurities at Grain Boundaries in Nanostructured ZnO Films

Daniela Ghica, Mariana Stefan,* Corneliu Ghica, and George E. Stan

National Institute of Materials Physics, P.O. Box MG-7, Magurele-Ilfov, 077125 Romania

Supporting Information

ABSTRACT: Magnetic and electrical properties of the nanostructured ZnO films are affected by the nonrandom distribution of impurities in the film due to segregation at grain boundaries (GBs) or extended defects. However, mapping the nature and distribution of the impurities in the film is not trivial. Here we demonstrate a simple, statistically relevant, and nondestructive procedure of quantitative determination of the paramagnetic impurities segregated at the GBs in nanostructured semiconducting and insulating films. From correlated electron paramagnetic resonance and transmission electron microscopy investigations, we determined the localization of trace amounts of Mn^{2+} ions, present as native impurities in a ZnO film deposited by magnetron sputtering at room temperature. In the as-deposited ZnO film, the Mn^{2+} ions were all localized in nanosized pockets of highly disordered ZnO dispersed between nanocrystalline columns. After the samples had been annealed in air at >400 °C, the size of the intercrystalline region decreased and the diffusion in GBs was activated, resulting in the localization of a portion of the Mn^{2+} ions in the peripheral atomic layers of the ZnO columns neighboring the GBs. The proportion of Mn^{2+} ions still localized at the GBs after annealing at 600 °C was 37%. The proposed method for the assessment of the presence and nature of impurities and the quantitative evaluation of their distribution in semiconducting and insulating nanostructures is expected to find direct applications in nanotechnology, in the synthesis and quality assurance of thin films for spintronics and opto- and nanoelectronics.

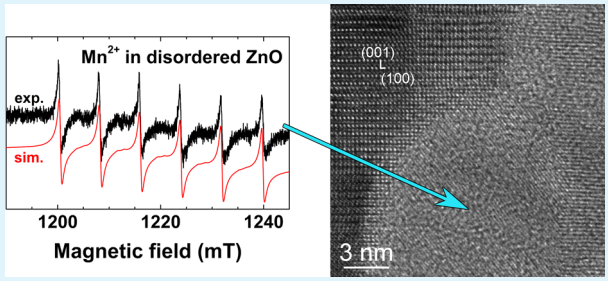

KEYWORDS: *nano-ZnO, thin films, microstructure, Mn^{2+} segregation, electron paramagnetic resonance, high-resolution transmission electron microscopy*

1. INTRODUCTION

The wide-band gap (3.37 eV) transparent semiconductor ZnO is presently one of the most studied materials following the prediction of room-temperature ferromagnetism (RTF) in p-type Mn-doped ZnO.[1] However, despite intensive research in this field over the past decade, both the existence and the origin of the RTF in diluted magnetic semiconductors (DMS) are still controversial.[2−5] Recent reviews[3,4] concluded that the observed RTF could be an effect of a nonrandom distribution of the magnetic ions, in many cases aggregated into ferromagnetic/metallic nanoclusters in the semiconductor host, or even of an experimental artifact such as contamination, because randomly distributed localized ions/spins could not actually produce RTF. Indeed, extensive surveys of the existing literature have shown that epitaxial ZnO films doped with magnetic ions such as Mn or Co were paramagnetic and RTF manifested only in nanostructured ZnO films, associated with grain boundaries (GBs), surfaces, or interfaces.[5]

In fact, there are several emergent phenomena at oxide interfaces, expected to offer scientific and technological opportunities in the coming years: interface ferromagnetism, superconductivity, quantum Hall effect, etc.[6,7] In particular, in ZnO nanostructures, the observed interface ferromagnetic and electrical properties[8,9] could be exploited in spintronics and nanoelectronics. Although such applications are still a challenge, undoped and doped ZnO structures, particularly as thin films, have already been successfully used for many other applications in optics, electronics, solar cells, sensors, energy, medicine, etc.[10−13] The uniform doping of thin films is very important for most applications, but as Droubay et al.[14] have shown, even highly soluble ions such as Mn^{2+} in ZnO, expected to be randomly distributed in an epitaxial film, have a propensity to cluster. In nanostructured films, the impurity distributions are usually nonuniform, because of segregation at GBs, extended defects, and interfaces. The segregation process at interfaces and GBs is the subject of intensive research, because of the way in which it affects the mechanical, electrical, and magnetic properties of the materials.[15−18] However, the actual determination of the amount of impurities segregated at the GBs is not trivial. To the best of our knowledge, such determinations are usually performed on sliced and/or fractured materials[15,17,19] and for impurity concentrations of >1%. Only recently have such studies been performed for lower

Received: June 4, 2014
Accepted: August 4, 2014
Published: August 4, 2014

impurity concentrations, but with quite elaborate and time-consuming methods.[15,17]

We propose electron paramagnetic resonance (EPR) spectroscopy as a reliable technique for studying segregation processes of impurity/dopant ions in insulating and semiconducting materials, as it can accurately determine both the nature and localization of the paramagnetic impurities.[20] The EPR spectra are extremely sensitive to small changes in the nature and configuration of the neighboring ligand atoms/ions, being able to offer a wealth of information about the local structure and composition of the lattice host. As recently shown in the case of semiconducting Zn-based nanocrystals doped with manganese at concentrations from several parts per million to 0.5%,[21−23] with this method we were able to determine the core or surface localization of the Mn^{2+} impurities and the formation of aggregates.

In the case of epitaxial Mn-doped ZnO films, detailed EPR studies showed the substitutional incorporation of low concentrations of isolated Mn^{2+} ions at Zn^{2+} sites.[4,24,25] However, the previously reported EPR investigations of nanostructured Mn-doped ZnO films failed to clearly determine the localization of the Mn^{2+} ions, because of the high doping levels used, at least 1% order of magnitude. At such concentrations, the competing dipolar and exchange interactions determine the excessive EPR line broadening, with the inevitable loss of information about the doping ion localization.

We have investigated the segregation process of the Mn^{2+} ions present at low concentrations (∼1 ppm) in nanostructured ZnO films prepared by RF magnetron sputtering at room temperature (RT). From correlated EPR and transmission electron microscopy/high-resolution transmission electron microscopy (TEM/HRTEM) investigations, we have determined the localization of the Mn^{2+} ions in the as-deposited and thermally treated nanostructured ZnO thin film. We have evidenced the segregation of the Mn^{2+} ions in the intercrystalline region (IC) in the as-deposited film as well as their slow diffusion in the GBs in the pulse-annealed ZnO film. From the EPR spectra, we have estimated the proportion of Mn^{2+} ions still localized in the GBs or diffused into the peripheral atomic layers of the ZnO columns neighboring the GBs after annealing.

As our results show, EPR offers a simple method for directly determining the amount of paramagnetic impurity ions segregated at the GBs in a nondestructive manner, even for very low impurity concentrations. The method is also statistically relevant, as it measures the whole film volume and very useful for determining the preparation conditions of nanostructured films with specific doping levels and/or impurity distributions for envisaged applications.

2. MATERIALS AND METHODS

ZnO thin films were synthesized onto r-cut sapphire substrates by RF magnetron sputtering in a UVN-75R1 (1.78 MHz) deposition system. The target was prepared by pressing pure ZnO powder (Sigma-Aldrich, puriss., product no. 14439) into a compact pellet. Film deposition was conducted for 3 h at a pure argon pressure of 0.3 Pa, with a RF power of ∼80 W. The substrate temperature was dependent on only plasma self-heating, reaching ∼80 °C.

The crystalline structure of the films was determined by X-ray diffraction (XRD), using a Bruker D8 Advance diffractometer, in parallel beam setting, equipped with a copper anode X-ray tube. The TEM/HRTEM investigations were performed on a JEOL ARM 200F high-resolution electron microscope operated at 200 kV.

X-Band (9.5 GHz) and Q-band (34 GHz) EPR experiments were performed at RT, in the Research Center for Advanced ESR/EPR Techniques (CetRESav) of the National Institute of Materials Physics. Details about the equipment and magnetic field calibration procedures can be found in ref 21 and at http://cetresav.infim.ro/. EPR measurements have been performed on both as-deposited and pulse-annealed ZnO films. For the pulse annealing experiments, the film inserted in the EPR tube was annealed in air in a temperature-stabilized (±1 °C) furnace at set temperatures of 300, 400, 500, and 600 °C. The sample was kept at the set temperature for 15 min and afterward cooled to RT where the EPR spectrum was recorded. The annealing temperatures and/or durations were selected to facilitate comparison with similar experiments on ZnO nanopowders[26] and nanostructured ZnO films deposited by magnetron sputtering at RT on SiO_2/Si substrates.[27]

Details regarding the thin film deposition procedure and the various characterization techniques are given in the Supporting Information.

3. RESULTS AND DISCUSSION

3.1. XRD and TEM/HRTEM Characterization of the ZnO Film. The XRD pattern of the ZnO film deposited on r-cut sapphire (Figure 1) shows the formation of a single-phase

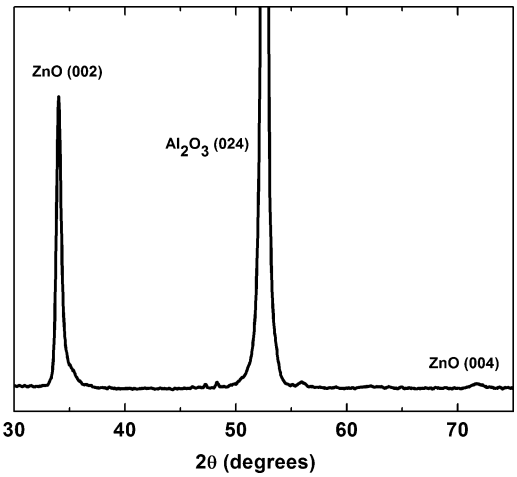

Figure 1. XRD diffractogram of the ZnO thin film deposited on r-cut sapphire.

nanostructured ZnO layer, strongly textured around the *c*-axis [corresponding to the (002) peak] (see JCPDS Card No. 89-1397). An average size of 19 nm has been calculated for the coherence domains along [001], taking into account the instrumental contribution to the peak broadening. Because the nonuniform strain contribution cannot be estimated, as only one peak is clearly observed, only the minimum value of the grain size along [001] can be calculated, considering a fully relaxed film.

However, using the procedure detailed in ref 27, we could evaluate *c*-axis strain ε_{zz} and the biaxial compressive stress. The obtained ε_{zz} of 1% indicates an out-of-plane tensile strain for an estimated in-plane biaxial compressive stress of 4.6 GPa, which is similar to those previously calculated.[27] The out-of-plane tensile strain corresponds to a shift toward smaller angles of the ZnO(002) diffraction peak, with respect to its position in the diffractogram of the ZnO powder used to prepare the sputtering targets. The asymmetry of the ZnO(002) peak points to a partial relaxation of the thin film, most probably in the topmost region.

The TEM image in Figure 2a shows the typical columnar growth of the ZnO film with a thickness of ∼580 nm,

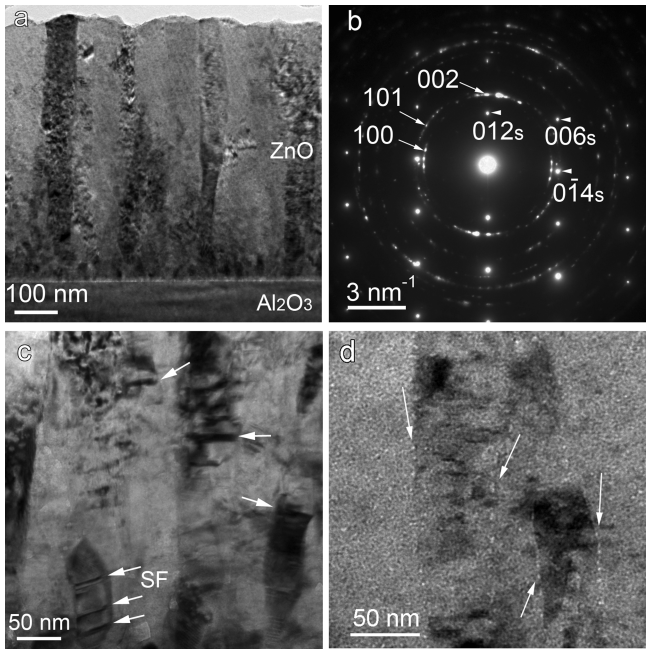

Figure 2. (a) Low-magnification cross-section TEM image showing the columnar growth of the ZnO thin film. (b) Selected area electron diffraction pattern revealing the textured growth of the ZnO layer and crystallographic orientation with respect to the sapphire substrate (subscript s indices). (c) Stacking faults inside the ZnO columns generating strain contrast. (d) Imperfect contact between the ZnO crystal grains, with rows of nanometric pockets trapped at the interfaces.

consisting of densely packed ∼50 nm wide columns. The electron diffraction pattern in Figure 2b corresponds to a selected area that includes the ZnO layer and the substrate. The diffraction spots denoted with a subscript s belong to the sapphire substrate.

The electron diffraction pattern confirms that the ZnO film is highly textured along the *c*-axis (direction of rapid growth for ZnO), according to the following dominant crystallographic orientation relation with respect to the substrate: $(001)_{ZnO}\|(012)_s$ and $(100)_{ZnO}\|(0\bar{1}4)_s$.

Strain contrast decorating the ZnO columns can be observed at low magnifications. In our opinion, the origin of the strain can be explained by the following film growth mechanism. During the first stages of film growth, ZnO crystal grains with a rather random orientation are nucleated on top of the sapphire substrate. Because ZnO exhibits a direction of rapid growth along the hexagonal *c*-axis, only those ZnO nanograins having the *c*-axis oriented almost perpendicular to the substrate are favored to grow, giving the [001] film texture. Neighboring grains with the *c*-axis slightly tilted away from the substrate normal [contributing to ZnO(002) peak broadening] will come into contact, exerting pressure upon each other and hence leading to the buildup of the in-plane biaxial compressive stress. An additional contribution to the biaxial stress comes from the lateral growth of the ZnO columns. As observed on the low-magnification TEM micrographs, the ZnO columns are significantly broader in the topmost region compared to the bottom part of the film. The accumulating in-plane compressive stress leads, on one hand, to out-of-plane tensile strain as measured by XRD. On the other hand, it is partially relaxed by the formation of planar defects (mainly stacking faults) along the hexagonal basal plane of ZnO, as shown by the TEM/HRTEM micrographs. The presence of the mentioned stacking faults inside the ZnO columns can be observed at higher magnifications (Figure 2c). Diffraction contrast imaging in the thinnest areas of the TEM specimen reveals also the imperfect contact between the ZnO columns. Thus, in Figure 2d, rows of nanometric pockets (2−5 nm in diameter), exhibiting brighter contrast in underfocused objective lens conditions, can be noticed lined up along the interfaces between the ZnO columns.

High-resolution TEM imaging of the ZnO crystal grains confirms the presence of the stacking faults (Figure 3a) and, on the other hand, reveals the presence of the amorphous phase at the interfaces between the columns, especially inside the nanoscaled pockets trapped between the growing ZnO columns. Figure 3b presents the interface between two ZnO crystal grains, namely, grain A oriented along the [−120] zone axis [the (001) and (100) planes are indicated in the figure] and grain B [the (101) planes are indicated in the figure]. The area denoted C between grains A and B contains the amorphous or poorly crystallized phase.

These nanometric pockets filled with amorphous phase at the GBs are no longer observed in the sample annealed at 600 °C for 45 min. The thermal treatment determined a process of atomic reordering of the GBs, and the interfaces of the ZnO columns became fully crystallized. The illustrating HRTEM image in Figure 3c shows the contact between three ZnO crystal grains in various crystallographic orientations, with no amorphous phase at the interface. However, the TEM observations did not allow us to detect a noticeable evolution of the density of structural defects after the thermal treatment.

3.2. EPR Investigation. The Q-band EPR spectrum of the as-grown ZnO film consists of six isotropic lines attributed to a very small amount of Mn^{2+} ions present as an unintended impurity in ZnO (Figure 4), as well as several anisotropic lines from the Cr^{3+} impurity in the single-crystal sapphire substrate. The X-band spectrum contains only the Cr^{3+} lines, showing that the amount of Mn^{2+} ions in the film is below the nominal detection limit of the X-band spectrometer of $\sim 2.5 \times 10^9$ spins/G. Given the volume of the ZnO film in the measured sample, of $\sim 8.4 \times 10^{-3}$ mm^3, we can estimate the concentration of Mn^{2+} ions in the ZnO film to be on the order of 1 ppm.

The low concentration of doping Mn^{2+} ions is expected to ensure their incorporation into the host lattice as isolated ions, allowing an accurate determination of the localization of Mn^{2+} ions in the ZnO film. Also, a low concentration of Mn^{2+} impurity ions does not affect the grain growth process in the nanostructured ZnO, which has an activation energy of ∼23 kJ/mol for both undoped ZnO and ZnO doped with a low Mn^{2+} concentration.[26] Therefore, the Mn^{2+} ions can be used to probe the annealing induced changes in the nanostructured ZnO lattice, associated with a crystallization process.

To evaluate the transfer of the impurities from the target to the film, we have also measured an amount of ZnO powder used to prepare the sputtering target. According to the manufacturer, the powder contains a maximal $KMnO_4$ level of 50 ppm. As the target was prepared by pressing the ZnO powder into a compact pellet, without further sintering, it is assumed that the distribution of the impurity in the target is similar to its distribution in the original powder. No EPR spectra from isolated manganese ions could be observed from the ZnO powder in the X- or Q-band, showing that the Mn^{2+} ions observed in the ZnO film were formed during the sputtering. The amount of Mn^{2+} in the film is 1 order of

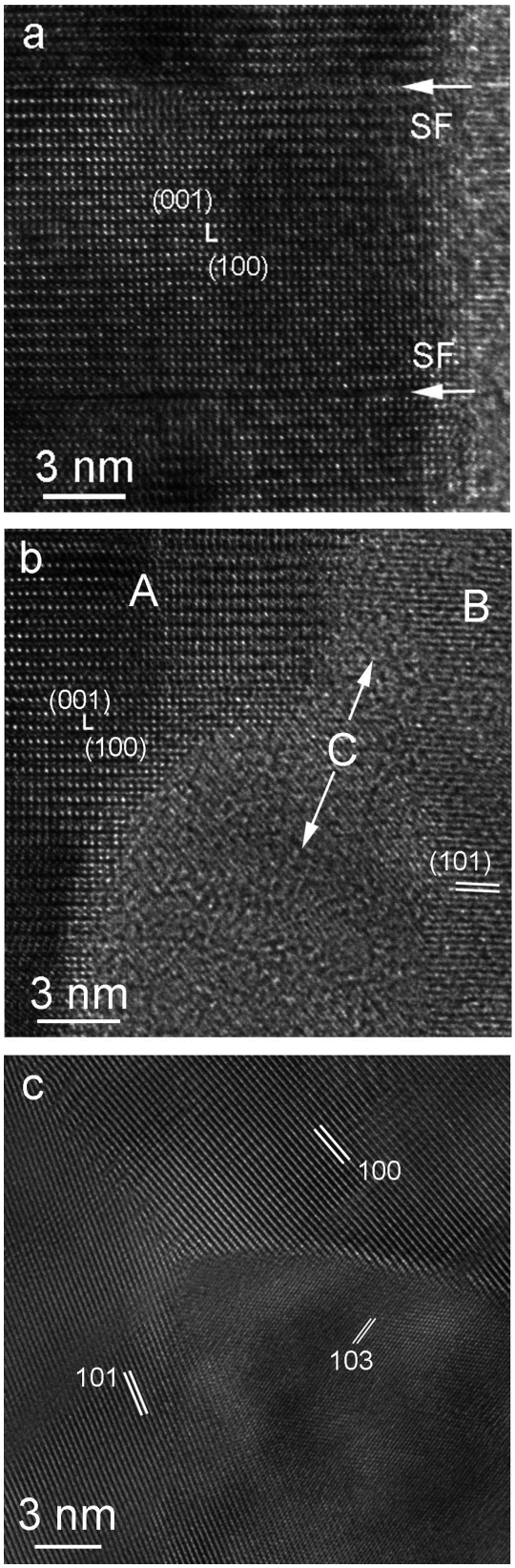

Figure 3. (a) HRTEM image of the as-deposited ZnO film showing the presence of stacking faults inside the ZnO columns. (b) Amorphous or poorly crystallized phase at the interface between the ZnO columns in the as-deposited film. (c) Fully crystallized interfaces between the ZnO columns after annealing at 600 °C for 45 min.

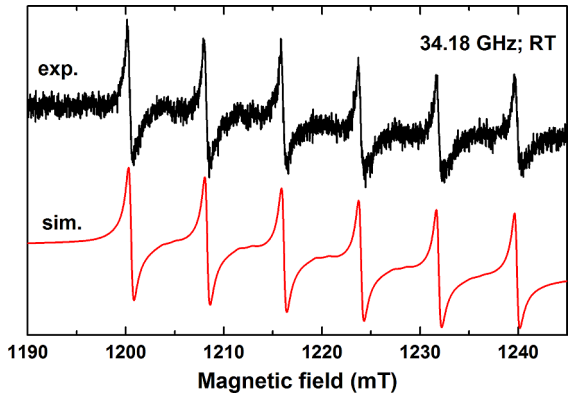

Figure 4. Experimental (exp.) Q-band EPR spectrum (20 scans) of the ZnO film and the simulated spectrum (sim.) for substitutional Mn^{2+} ions.

magnitude smaller than the nominal manganese amount in the target, which could be due to a nonstoichiometrical transfer from the target to the film, or to the presence of EPR silent manganese ions.

The analysis of the EPR spectra of the Mn^{2+} ions was performed with the spin Hamiltonian (SH) and line shape simulation procedure presented in the Supporting Information, developed for nanopowder samples. The SH parameter values determined for the Mn^{2+} ions in the as-deposited ZnO film (Table S1 of the Supporting Information) match the values reported in ref 22 for the Mn^{2+}-d centers in ZnO nanopowders and correspond to the substitutional localization of the impurity ions at Zn^{2+} sites in disordered regions of the ZnO film. The EPR spectrum simulated with these SH parameters is displayed in Figure 4 and reproduces well the experimental spectrum.

As seen from the HRTEM image (Figure 3b), in the as-deposited film there are nanometer-sized pockets of disordered ZnO dispersed between the ZnO grains. Therefore, as revealed by the EPR data, in the ZnO films prepared at RT by RF magnetron sputtering, the Mn^{2+} impurity ions do not enter the crystallized ZnO nanograins and are all gathered in the IC region at the GBs.

When the ZnO film is annealed in air, the line shape of the EPR spectrum of Mn^{2+} changes progressively, signaling a change in the environment of the Mn^{2+} ions (Figure 5). The EPR spectrum after the 300 °C annealing is similar to that of the as-deposited film. For pulse annealing temperatures (T_{ann}) of ≥400 °C, another Mn^{2+} spectrum starts to grow, while the intensity of the Mn^{2+}-d spectrum from the disordered ZnO decreases.

As the recorded Mn^{2+} EPR spectra remained isotropic after all annealing steps, we have employed the same line shape simulation procedure for the determination of the SH parameters of the new observed Mn^{2+} centers. We have determined their SH parameters from the EPR spectrum measured after annealing the ZnO film at 600 °C for an additional 30 min (annealing for 45 min at 600 °C in total), which was recorded with 20 scans for a better resolution (Figure 6). They are further called Mn^{2+}-c centers, as they resemble the Mn^{2+}-c centers in ZnO nanocrystals[22] in both SH parameter values (Table S1 of the Supporting Information) and behavior. We should mention that all the experimental spectra displayed in Figures 4–6 were recorded for an orientation of the static magnetic field parallel to the film plane, with an error

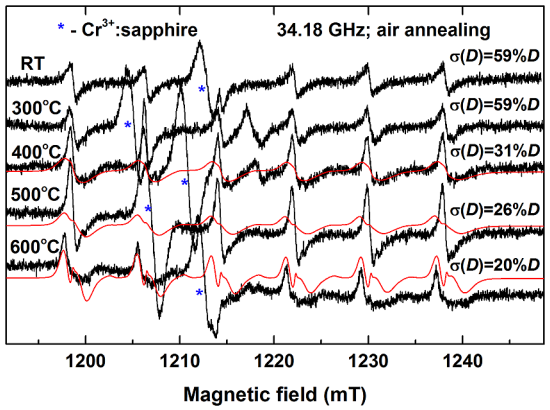

Figure 5. Thick black lines are experimental Q-band EPR spectra (five scans) of the ZnO film annealed for 15 min in air at the indicated annealing temperatures. Thin red lines are simulations of the Mn^{2+}-c EPR spectra with different broadening parameter $\sigma(D)$ values. The EPR lines of the Cr^{3+} ions from the sapphire substrate are marked with blue asterisks.

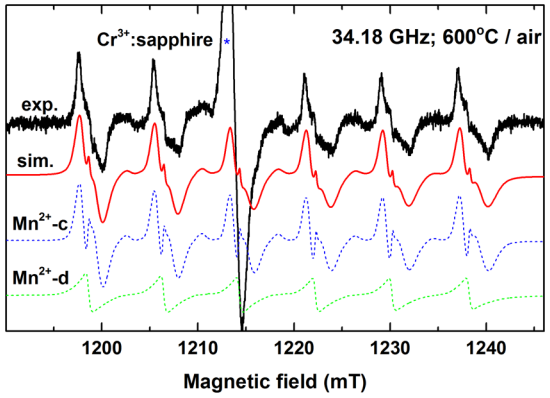

Figure 6. Experimental (exp., 20 scans) and simulated (sim.) Q-band EPR spectra of the ZnO film annealed in air at 600 °C for 45 min. The dotted lines are the calculated spectra of the Mn^{2+} in the nanocrystalline (Mn^{2+}-c) and disordered (Mn^{2+}-d) ZnO. The EPR lines of the Cr^{3+} ions from the sapphire substrate are marked with blue asterisks.

of <5°, because a better signal-to-noise ratio was obtained under these conditions.

Using the determined SH parameters, we have simulated the EPR spectra of the Mn^{2+}-c centers in the ZnO film annealed at different temperatures from Figure 5. Each experimental spectrum contains the contributions of both Mn^{2+}-c and Mn^{2+}-d centers, as shown in detail in Figure 6. However, in Figure 5, only the simulation of the Mn^{2+}-c centers is represented, to highlight their evolution with the annealing temperature. The intensity and line broadening of the Mn^{2+}-c spectrum change with increasing annealing temperature, pointing to structural transformations in the annealed ZnO film. The EPR line broadening parameter $\sigma(D)$, as defined in the Supporting Information, is a measure of the local strain. The EPR spectrum intensity of a center, calculated by the double integration of the spectrum, is proportional to the concentration of the respective center in the host lattice. Therefore, the changes in the relative intensities of the two centers with the annealing temperature show the increase in the Mn^{2+}-c center concentration at the expense of the Mn^{2+}-d centers. Considering the initial localization of the Mn^{2+} ions in the disordered IC region, such changes can be explained by the crystallization of the disordered ZnO phase and/or the diffusion of the Mn^{2+} ions into the crystallized grains.

If we define f_c and f_d as the concentration fractions in percent of the Mn^{2+} ions in the crystalline and disordered ZnO phases, respectively, where $f_c + f_d = 100\%$, the double integration of the simulated spectra of the Mn^{2+}-c and Mn^{2+}-d centers represented in Figure 6 results in $f_c = 63\%$ and $f_d = 37\%$. The accuracy of this result is limited by the errors in the fitting of the total experimental spectrum (5%, due to the low signal-to-noise ratio) and in the evaluation of the relative intensity of the spectra of Mn^{2+} ions in nanocrystals and at the GBs (up to 2%).

As seen in Table S1 of the Supporting Information, the value of the D parameter for the Mn^{2+}-c centers in the annealed ZnO film is smaller than in the ZnO nanocrystals. According to ref 24, the D parameter absolute value varies in correlation with the manganese concentration in the ZnO host, decreasing with the increase in the doping level. Because the ionic radius of Mn^{2+} in tetrahedral coordination (0.80 Å) is greater than that of Zn^{2+} in tetrahedral coordination (0.74 Å), a larger concentration of dopant ions induces a distortion of the hexagonal lattice, which leads to changes in the local crystal field at the Mn^{2+} sites. In our case, the local concentration of Mn^{2+} impurities is expected to be considerably larger than the concentration in the target material, as the Mn^{2+} ions are localized in a very small fraction of the nanostructured ZnO film volume, namely only in the proximity of the GBs. Moreover, it is very likely that the Mn^{2+} ions are not the only impurities contributing to the distortion of the ZnO lattice in the GBs region. The Mn^{2+} ions are assumed to have a high solubility in the ZnO lattice, because of the match of their electric charge and ionic radius with the Zn^{2+} host cations, and thus, their incorporation only at the GBs is quite unexpected. The impurities with a segregation probability higher than that of Mn^{2+} due to the difference in their ionic radii and/or valences[28] are even more likely to be found in the regions of GBs. Such impurities are the K^+ ions, with an ionic radius (1.33 Å) considerably larger than that of the host cations and a different valence, that resulted from the decomposition of the $KMnO_4$ compound in the starting material. Therefore, the lower D parameter value of the Mn^{2+}-c centers in the nanostructured ZnO film is most likely associated with a higher local concentration of Mn^{2+} ions and other impurities (i.e., traces of K, Pb, Cd, and Fe cations and Cl^- anions, as listed by the producer, as well as EPR silent Mn ions) transferred from the target material to the film.

3.3. Discussion. Assuming that in the pulse-annealed film the disordered phase from the IC region suffers a crystallization process, the nucleation of the crystallized phase is expected to take place at the GBs. The decrease in the broadening parameter $\sigma(D)$ of the Mn^{2+}-c centers with the annealing temperature (Figure 5) reveals an ordering of the local host lattice around the Mn^{2+} ions, as the ordered phase grows. Our previous study of ZnO nanopowders showed that up to 400 °C the dominant growth process consists of the rearrangement of atoms at interfaces, driven by a decrease in the surface-induced strain.[26] Above this temperature, atom diffusion in the interfaces and GBs starts contributing as well to the grain growth, becoming the dominant process above 500 °C and leading to an increase in the larger grains at the expense of the smaller ones.

The broadening parameter $\sigma(D)$ of the Mn^{2+}-c centers in ZnO nanocrystals decreases with an increase in the average

crystallite size d as $\sigma(D) \sim \exp(-d/\delta)$, where δ is a constant.[26] When applying this empirical relation to the Mn^{2+}-c centers in the annealed ZnO film, assuming that they remain in the space of the original IC region and do not diffuse in the ZnO columns, from the calculated $\sigma(D)$ values listed in Figure 5, one would expect the newly formed ZnO grains to reach 5, 8, and 14 nm after being annealed at 400, 500, and 600 °C, respectively. In the case of the nanostructured films, the original pockets of disordered material are only a few nanometers wide. The surrounding GBs of the ZnO columns offer nucleation sites for the ZnO grains in the IC regions, but the growth of these grains is limited by the width of the disordered regions. While the presence of ∼5 nm grains after annealing at 400 °C is not unreasonable, the growth of larger grains seems not to be plausible. Moreover, under these annealing conditions, a recrystallization of the film, with the nucleation and growth of new grains at the expense of the original strained ones, is excluded, because for films with strain values of <1.4% the temperature threshold for recrystallization is >600 °C.[27]

A more reasonable explanation is that the ZnO columns have grown by the ordering of the atoms at the GBs, incorporating also the Mn^{2+} ions, especially at the temperatures at which atom diffusion in the GBs is activated. Indeed, as observed by HRTEM (section 3.1 and Figure 2), after annealing at 600 °C, the crystallized ZnO columns are separated by well-defined GBs, without any inclusions of poorly crystallized material. The activation energy of the diffusion process in the GBs, ∼79 kJ/mol, is considerably smaller than the bulk diffusion activation energy.[29,30] The observed variation of the broadening parameter of the Mn^{2+}-c centers with the annealing temperature reflects thus the diffusion of the Mn^{2+} ions in the GBs. As an additional argument in favor of this hypothesis, the diffusion of the Mn^{2+} ions is expected to lead to an increase in the distances between the ions and thus a decrease of the dipolar interaction, reflected in the decrease in the individual EPR line width of the Mn^{2+} spectra from 0.4 mT in the disordered phase to 0.15 mT in the crystalline phase after annealing at 600 °C (see Table S1 of the Supporting Information).

Considering the spectrum in Figure 6, the longer annealing time did not affect the local strain "seen" by the Mn^{2+} ions, showing that their diffusion is quite slow at this temperature. Indeed, both Mn^{2+}-c and Mn^{2+}-d spectra do not change in either intensity or line broadening before or after the supplementary 30 min annealing at this temperature. Our results are consistent with those of Puchert et al.,[27] showing that the compressive strain decreases approximately linearly with the annealing temperature, and at 630 °C, most of the structural changes occur within the first 10 min of annealing. According to their data, annealing at 600 °C should lead to a quite low biaxial compressive strain (∼1 GPa) and an average crystallite size of ∼30 nm. The rather large lattice strain sensed by the Mn^{2+}-c centers, reflected by the 20% D value of the broadening parameter $\sigma(D)$, can be explained only by the localization of the Mn^{2+} ions in the more disordered regions near the GBs, as expected when this diffusion process is the dominant one.

We can conclude that, after annealing at 600 °C, the Mn^{2+} ions remain nonhomogeneously distributed within the film, 37% of them remaining at the GBs while the rest are localized in the peripheral atomic layers of the ZnO columns, close to the GBs. The presence of extended defects could facilitate the migration of the impurities inside the grains,[31] but they cannot ensure a uniform distribution either.

We should mention at this point that our nanostructured ZnO film with such a low concentration of Mn^{2+} ions constitutes a simplified case study, with only two clear localizations of the Mn^{2+} ions. For higher impurity concentrations, other phenomena could become observable, leading to more information about the distribution and behavior of the impurities. Thus, if enough impurity ions penetrate in the more ordered regions from the nanocolumn core, the film texture could lead to anisotropic spectra from these impurities. Another possible effect, especially for aliovalent impurities, is the aggregation of the impurities during annealing, usually reflected in a dipolar broadening of the EPR lines.

To the best of our knowledge, this is the first EPR quantitative estimation of the segregation of paramagnetic impurities in nanostructures. As mentioned in the Introduction, the analysis of the segregation of impurities at GBs is not trivial, and the commonly used methods (Auger electron spectroscopy, secondary ion mass spectroscopy, analytical electron microscopy, field ion microscopy, or atom probe tomography) involve slicing and/or fracturing the materials, need impurity concentration levels of >1%, and/or lack statistical relevance.[15,17,19] Recently, Wang et al.[15] have identified very low impurity concentrations by HRTEM imaging, associated spectroscopic techniques, and first-principles calculations. They have thus obtained spatial distribution information and identified nonparamagnetic impurities, as well, but their very complex method raises a statistical problem, as the investigated sample volume was very small.[15] Herbig et al.[17] used correlated atom probe tomography and TEM with an optimized setup to realize a statistically robust analysis of the GB segregation space. Although very informative, the method is very complex and time-consuming. Comparatively, our method applies only to paramagnetic impurities, at sufficiently low concentrations (<1%) to have small dipolar interactions and consequent line broadening, and does not provide crystallographic information about the GB space. However, its simplicity and nondestructive aspect, as well as its statistical relevance, speak in its favor. It also shows a relatively simple and less time-consuming manner for establishing the optimal preparation conditions, such as temperature, annealing duration, and atmospheric composition, for nanostructured films with a desired structure and impurity distribution. Indeed, EPR provides a ready feedback not only about the type and localization of the dopants but also about the phases present in the nanostructures prepared by various methods, with an accuracy level that is often not available with structural methods such as XRD or TEM.[23] The proposed EPR-based method of evaluation of the presence and distribution of impurities could thus be adapted as a regular test for the quality assurance of the defect-engineered thin films.

We emphasize that this method is not restricted only to the Mn^{2+} impurity but can be applied to other combinations of paramagnetic impurity and nanostructured semiconductor or insulating host, as it is based on the sensitivity of the paramagnetic ions to the local strain or disorder in the host lattice. For example, dependencies of the EPR line broadening parameter on the nanoparticle size, similar to that observed for Mn^{2+} in ZnO, have been observed in several other systems of technological interest: Cr^{+} in $PbTiO_3$,[32] Fe^{3+} in ZnO,[33] and Gd^{3+} in LaF_3.[34]

We should also mention that the experimental results of this study offer answers to some important questions with regard to the properties of doped nanostructured thin films. First, they confirm previous theoretical studies of the segregation in GBs of higher concentrations of dopants in nanostructures.[35,36] Thus, on the basis of the Mn solubility limit in ZnO, shown to be dependent on grain size, Straumal et al.[35] have concluded that in Mn-doped nanograined ZnO films the dopant accumulates at the GBs in Mn-enriched layers, consisting of several monolayers. Our study confirms and extends the validity of their results toward low dopant concentrations and provides an instrument for directly monitoring the variation with the annealing of the distribution of impurity ions in the ZnO film.

Second, our results suggest another possible origin of the RTF observed in nominally pure or doped with nonmagnetic ions ZnO nanostructures, along with the generally attributed one, namely intrinsic defects such as oxygen and/or zinc vacancies.[37−40] As we have shown here, the low concentrations of unintentional impurities in the starting material could become, by the accumulation of impurities at the GBs, local concentrations that are sufficiently high to give rise to dipolar and exchange interactions between the impurity ions, thus affecting the magnetic properties. In the case of intentional doping, the nonuniform localization of the impurities in the IC region close to the GBs could seriously influence not only the magnetic properties of the nanostructured ZnO films[5] but also their electrical conductivity and photoluminescence. As all possible applications in spintronics and opto- and nanoelectronics require the control of these properties in nanostructures, the identification of their origin is of paramount importance.

We emphasize that these results were obtained for nanostructured ZnO films deposited by RF magnetron sputtering at RT. Differences in the preparation method of the films will very likely affect the incorporation of dopants. Thus, heating the substrate is expected to affect the film growth and morphology, as well as the diffusion of the impurities in the film. Films prepared by wet chemistry methods could have a more uniform distribution of impurities in the lattice, which is important for applications in optoelectronics. In each case, similar investigations of the incorporation of dopants like that presented here could be performed, for an informed selection of the appropriate preparation method of the films for specific applications.

4. CONCLUSIONS

The localization of Mn^{2+} ions in ZnO nanostructured films containing only traces of Mn impurity ions (∼1 ppm) was investigated by correlated EPR, XRD, and TEM/HRTEM techniques. We have experimentally demonstrated by EPR that in a nanostructured ZnO thin film, even at a very low Mn concentration, all the Mn^{2+} ions accumulate in the disordered regions of the film. As seen by HRTEM, such regions correspond to nanometric pockets filled with amorphous phase along the GBs. To the best of our knowledge, this is the first direct observation of the complete segregation at GBs of very low impurity concentrations, and also the first time that EPR was used to probe the segregation process.

We have also shown that even after thermal annealing at 600 °C for 45 min, when equilibrium was achieved, the distribution of the Mn^{2+} ions is still nonuniform in the nanostructured ZnO film, 37% of the Mn^{2+} ions remaining at the GBs, while the rest are localized in the peripheral strained regions of the ZnO columns neighboring the GBs. Our results demonstrate a simple, statistically relevant, and nondestructive procedure for evaluating the amount of paramagnetic impurities segregated at the GBs in a nanostructured film, which can be further used to establish the preparation conditions for films designed for specific applications. Moreover, the proposed EPR-based method can be adapted as a regular test for the quality assurance of the defect-engineered thin films. Such applications could be of real interest for nanotechnology. The limitations of this method are, as shown, that it can be applied only for paramagnetic impurities at concentrations of <1%, for which the dipolar interactions do not wipe out the relevant information in the EPR spectra.

Our findings are highly important with regard to any application involving doped nanostructured ZnO films, as they show that even in nominally pure films the native impurities could accumulate in quite high local concentrations at the GBs, being able to affect the magnetic and electrical properties of the films. This effect could be further controlled by defect engineering for specific applications. We expect that these results are of interest for a broad research and technology community, as they can help improve the knowledge for top applications in spintronics and opto- and nanoelectronics.

■ ASSOCIATED CONTENT

Ⓢ Supporting Information

Details about the thin film deposition procedure and characterization methods, analysis of EPR spectra, and a table of EPR spectral parameters of the Mn centers in various ZnO structures. This material is available free of charge via the Internet at http://pubs.acs.org.

■ AUTHOR INFORMATION

Corresponding Author

*Phone: 0040 213690185. Fax: 0040 213690177. E-mail: mstefan@infim.ro.

Notes

The authors declare no competing financial interest.

■ ACKNOWLEDGMENTS

This work was supported by UEFISCDI through Projects PN-II-ID-PCCE-2011-2-0006 (Contract 3/2012) and PN-II-ID-PCE-2012-4-0362 (Contract 36/2013).

■ REFERENCES

(1) Dietl, T.; Ohno, H.; Matsukura, F.; Cibert, J.; Ferrand, D. Zener Model Description of Ferromagnetism in Zinc-Blende Magnetic Semiconductors. *Science* **2000**, *287*, 1019−1022.

(2) Sundaresan, A.; Rao, C. N. R. Ferromagnetism as a Universal Feature of Inorganic Nanoparticles. *Nano Today* **2009**, *4*, 96−106.

(3) Dietl, T. A Ten-Year Perspective on Dilute Magnetic Semiconductors and Oxides. *Nat. Mater.* **2010**, *9*, 965−974.

(4) Mauger, A. No Intrinsic Ferromagnetism in Transition-Metal-Doped ZnO: An Electron Paramagnetic Resonance Analysis. *Appl. Magn. Reson.* **2010**, *39*, 3−29.

(5) Coey, J. M. D.; Mlack, J. T.; Venkatesan, M.; Stamenov, P. Magnetization Process in Dilute Magnetic Oxides. *IEEE Trans. Magn.* **2010**, *46*, 2501−2503.

(6) Hwang, H. Y.; Iwasa, Y.; Kawasaki, M.; Keimer, B.; Nagaosa, N.; Tokura, Y. Emergent Phenomena at Oxide Interfaces. *Nat. Mater.* **2012**, *11*, 103−113.

(7) Lee, J.-S.; Xie, Y. W.; Sato, H. K.; Bell, C.; Hikita, Y.; Hwang, H. Y.; Kao, C.-C. Titanium d_{xy} Ferromagnetism at the $LaAlO_3/SrTiO_3$ Interface. *Nat. Mater.* **2013**, *12*, 703−706.

(8) Straumal, B. B.; Mazilkin, A. A.; Protasova, S. G.; Myatiev, A. A.; Straumal, P. B.; Schütz, G.; van Aken, P. A.; Goering, E.; Baretzky, B. Magnetization Study of Nanograined Pure and Mn-Doped ZnO Films: Formation of a Ferromagnetic Grain-Boundary Foam. *Phys. Rev. B* **2009**, *79*, 205206.
(9) Chuang, M.-Y.; Chen, Y.-C.; Su, Y.-K.; Hsiao, C.-H.; Huang, C.-S.; Tsai, J.-J.; Yu, H.-C. Negative Differential Resistance Behavior and Memory Effect in Laterally Bridged ZnO Nanorods Grown by Hydrothermal Method. *ACS Appl. Mater. Interfaces* **2014**, *6*, 5432−5438.
(10) Ozgur, U.; Alivov, Ya. I.; Liu, C.; Teke, A.; Reshchikov, M. A.; Dogan, S.; Avrutain, V.; Cho, S.-J.; Morkoc, H. A Comprehensive Review of ZnO Materials and Devices. *J. Appl. Phys.* **2005**, *98*, 041301.
(11) Schmidt-Mende, L.; MacManus-Driscoll, J. L. ZnO: Nanostructures, Defects and Devices. *Mater. Today* **2007**, *10*, 40−48.
(12) Fortunato, E.; Gonçalves, A.; Pimentel, A.; Barquinha, P.; Gonçalves, G.; Pereira, L.; Ferreira, I.; Martins, R. Zinc Oxide, a Multifunctional Material: From Material to Device Applications. *Appl. Phys. A: Solids Surf.* **2009**, *96*, 197−205.
(13) Hoye, R. L. Z.; Musselman, K. P.; MacManus-Driscoll, J. L. Research Update: Doping ZnO and TiO_2 for solar cells. *APL Mater.* **2013**, *1*, 060701 and references cited therein.
(14) Droubay, T. C.; Keavney, D. J.; Kaspar, T. C.; Heald, S. M.; Wang, C. M.; Johnson, C. A.; Whitaker, K. M.; Gamelin, D. R.; Chambers, S. A. Correlated substitution in paramagnetic Mn^{2+}-doped ZnO epitaxial films. *Phys. Rev. B* **2009**, *79*, 155203.
(15) Wang, Z.; Saito, M.; McKenna, K. P.; Gu, L.; Tsukimoto, S.; Shluger, A. L.; Ikuhara, Y. Atom-Resolved Imaging of Ordered Defect Superstructures at Individual Grain Boundaries. *Nature* **2011**, *479*, 380−383.
(16) Atanacio, A. J.; Bak, T.; Nowotny, J. Effect of Indium Segregation on the Surface versus Bulk Chemistry for Indium-Doped TiO_2. *ACS Appl. Mater. Interfaces* **2012**, *4*, 6626−6634.
(17) Herbig, M.; Raabe, D.; Li, Y. J.; Choi, P.; Zaefferer, S.; Goto, S. Atomic-Scale Quantification of Grain Boundary Segregation in Nanocrystalline Material. *Phys. Rev. Lett.* **2014**, *112*, 126103.
(18) Feng, Z.; Yacoby, Y.; Gadre, M. J.; Lee, Y.-L.; Hong, W. T.; Zhou, H.; Biegalski, M. D.; Christen, H. M.; Adler, S. B.; Morgan, D.; Shao-Horn, Y. Anomalous Interface and Surface Strontium Segregation in $(La_{1-y}Sr_y)_2CoO_{4\pm\delta}/La_{1-x}Sr_xCoO_{3-\delta}$ Heterostructured Thin Films. *J. Phys. Chem. Lett.* **2014**, *5*, 1027−1034.
(19) Popov, V. V.; Sergeev, A. V.; Arkhipova, N. K.; Istomina, A. Yu. Determination of the Parameters of Grain-Boundary Diffusion and Segregation of Co in W Using an Improved Model of Grain-Boundary Diffusion. *Phys. Met. Metallogr. (Transl. of Fiz. Met. Metalloved.)* **2011**, *112*, 256−266.
(20) Pilbrow, J. R. *Transition Ion Electron Paramagnetic Resonance*; Clarendon Press: Oxford, U.K., 1990.
(21) Stefan, M.; Nistor, S. V.; Ghica, D.; Mateescu, C. D.; Nikl, M.; Kucherkova, R. Substitutional and Surface Mn^{2+} Centers in Cubic ZnS:Mn Nanocrystals. A Correlated EPR and Photoluminescence Study. *Phys. Rev. B* **2011**, *83*, 045301.
(22) Nistor, S. V.; Nistor, L. C.; Stefan, M.; Ghica, D.; Aldica, Gh.; Barascu, J. N. Crystallization of Disordered Nanosized ZnO Formed by Thermal Decomposition of Nanocrystalline Hydrozincite. *Cryst. Growth Des.* **2011**, *11*, 5030−5038.
(23) Nistor, S. V.; Ghica, D.; Stefan, M.; Nistor, L. C. Sequential Thermal Decomposition of the Shell of Cubic $ZnS/Zn(OH)_2$ Core-Shell Quantum Dots Observed With Mn^{2+} Probing Ions. *J. Phys. Chem. C* **2013**, *117*, 22017−22028.
(24) Diaconu, M.; Schmidt, H.; Poeppl, A.; Boettcher, R.; Hoentsch, J.; Klunker, A.; Spemann, D.; Hochmuth, H.; Lorenz, M.; Grundmann, M. Electron Paramagnetic Resonance of $Zn_{1-x}Mn_xO$ Thin Films and Single Crystals. *Phys. Rev. B* **2005**, *72*, 085214.
(25) Chikoidze, E.; von Bardeleben, H. J.; Dumont, Y.; Galtier, P.; Cantin, J. L. Magnetic Interactions in $Zn_{1-x}Mn_xO$ Studied by Electron Paramagnetic Resonance Spectroscopy. *J. Appl. Phys.* **2005**, *97*, 10D316.
(26) Stefan, M.; Nistor, S. V.; Ghica, D. Correlation of Lattice Disorder with Crystallite Size and the Growth Kinetics of Mn^{2+} Doped ZnO Nanocrystals Probed by Electron Paramagnetic Resonance. *Cryst. Growth Des.* **2013**, *13*, 1350−1359.
(27) Puchert, M. K.; Timbrell, P. Y.; Lamb, R. N. Postdeposition Annealing of Radio Frequency Magnetron Sputtered ZnO Films. *J. Vac. Sci. Technol., A* **1996**, *14*, 2220−2230.
(28) Ingham, B.; Linklater, R.; Kemmit, T. Grain Growth Kinetics of ZnO:Al Nanocrystalline Powders During Calcination from Sol-Gels. *J. Phys. Chem. C* **2011**, *115*, 21034−21040.
(29) Tomlins, G. W.; Routbort, J. L.; Mason, T. O. Oxygen Diffusion in Single-Crystal Zinc Oxide. *J. Am. Ceram. Soc.* **1998**, *81*, 869−876.
(30) Tomlins, G. W.; Routbort, J. L.; Mason, T. O. Zinc Self-Diffusion, Electrical Properties, and Defect Structure of Undoped, Single Crystal Zinc Oxide. *J. Appl. Phys.* **2000**, *87*, 117−123.
(31) Nistor, S. V.; Stefan, M.; Nistor, L. C.; Goovaerts, E.; Van Tendeloo, G. Incorporation and Localization of Substitutional Mn^{2+} Ions in Cubic ZnS Quantum Dots. *Phys. Rev. B* **2010**, *81*, 035366.
(32) Erdem, E.; Bottcher, R.; Glasel, H. J.; Hartmann, E. Size Effects in Chromium-Doped $PbTiO_3$ Nanopowders Observed by Multi-Frequency EPR. *Magn. Reson. Chem.* **2005**, *43*, S174−S182.
(33) Açıkgöz, M.; Drahus, M. D.; Ozarowski, A.; van Tol, J.; Weber, S.; Erdem, E. Local Coordination of Fe^{3+} in ZnO Nanoparticles: Multi-Frequency Electron Paramagnetic Resonance (EPR) and Newman Superposition Model Analysis. *J. Phys.: Condens. Matter* **2014**, *26*, 155803.
(34) Gazizulina, A. M.; Alakshin, E. M.; Baibekov, E. I.; Gazizulin, R. R.; Zakharov, M. Yu.; Klochkov, A. V.; Korableva, S. L.; Tagirov, M. S. Electron Paramagnetic Resonance of Gd^{3+} Ions in Powders of LaF_3:Gd^{3+} Nanocrystals. *JETP Lett.* **2014**, *99*, 149−152.
(35) Straumal, B.; Baretzky, B.; Mazilkin, A.; Protasova, S.; Myatiev, A.; Straumal, P. Increase of Mn Solubility with Decreasing Grain Size in ZnO. *J. Eur. Ceram. Soc.* **2009**, *29*, 1963−1970.
(36) Lee, H. B.; Prinz, F. B.; Cai, W. Atomistic Simulations of Grain Boundary Segregation in Nanocrystalline Yttria-Stabilized Zirconia and Gadolinia-Doped Ceria Solid Oxide Electrolytes. *Acta Mater.* **2013**, *61*, 3872−3887.
(37) Sundaresan, A.; Bhargavi, R.; Rangarajan, N.; Siddesh, U.; Rao, C. N. R. Ferromagnetism as a Universal Feature of Nanoparticles of the Otherwise Nonmagnetic Oxides. *Phys. Rev. B* **2006**, *73*, 161306(R).
(38) Panigrahy, B.; Aslam, M.; Misra, D. S.; Ghosh, M.; Bahadur, D. Defect-Related Emissions and Magnetization Properties of ZnO Nanorods. *Adv. Funct. Mater.* **2010**, *20*, 1161−1165.
(39) Xia, Z.; Wang, Y.; Fang, Y.; Wan, Y.; Xia, W.; Sha, J. Understanding the Origin of Ferromagnetism in ZnO Porous Microspheres by Systematic Investigations of the Thermal Decomposition of $Zn_5(OH)_8Ac_2$-$2H_2O$ to ZnO. *J. Phys. Chem. C* **2011**, *115*, 14576−14582.
(40) Ghosh, S.; Khan, G. G.; Varma, S.; Mandal, K. Influence of Film Thickness and Oxygen Partial Pressure on Cation-Defect-Induced Intrinsic Ferromagnetic Behavior in Luminescent p-Type Na-Doped ZnO Thin Films. *ACS Appl. Mater. Interfaces* **2013**, *5*, 2455−2461.